A Probabilistic Shear Wave Velocity Model of the Crust in the Central West Australian Craton Constrained by Transdimensional Inversion of Ambient Noise Dispersion

Huaiyu Yuan[1,2,3] (iD) **and Thomas Bodin**[4] (iD)

[1]ARC Centre of Excellence for Core to Crust Fluid Systems, Department of Earth and Planetary Sciences, Macquarie University, Sydney, New South Wales, Australia, [2]Geological Survey of Western Australia, Mineral House, East Perth, Western Australia, Australia, [3]Centre for Exploration Targeting, University of Western Australia, Perth, Western Australia, Australia, [4]Université Lyon, Université Lyon 1, Ens de Lyon, CNRS, Villeurbanne, France

Abstract The Capricorn Orogen in central Western Australia played important roles in initializing and finalizing the West Australian craton. Surface geological mapping and isotopic studies show that the crust has recorded over a billion years of tectonic history spanning from its crustal formation in the Archean to episodes of tectonothermal events during the Proterozoic cratonization processes. The region therefore provides us with an ideal laboratory to characterize the seismic signature associated with tectonic processes. We constructed a crustal shear wave velocity model of the core region of the orogen, the Glenburgh Terrane and its north boundary, by inverting the array group velocity dispersion data measured from a high-density temporary array. A modified Bayesian transdimensional tomography technique, which incorporates a smooth-varying regional reference velocity model and Moho topography, was used to invert for the crustal velocity variations. The inverted velocity model adds great detail to the intracrustal structure and provides complementary seismic velocity information to refine the regional tectonic processes. Distinct patterns in the velocity structure support that the Glenburgh Terrane is an Archean microcontinent and favor the role of Paleoproterozoic subductions/accretions during the assembly of the West Australian Craton.

1. Introduction

The origin and evolution of Earth's crust, especially in Precambrian cratons, remain debatable research topics (e.g., DePaolo et al., 2008; National Research Council, 2012). The cratonic crust holds the oldest direct record of Earth's evolution (e.g., Wilde et al., 2001), but how it formed remains controversial. Distinct tectonic styles, for example, vertical accretion through mantle upwellings and horizontal accretion through modern-style subduction, are both suggested as the genesis of some of the earliest Archean crust (de Wit, 1998; Nutman et al., 2009; Van Kranendonk et al., 2004). When modern-style subduction started to operate also remains debated (Brown, 2008; Hamilton, 2007). It is suggested that due to missing critical subduction-related information in early geological records, model style subduction may only initiate in the late Precambrian (e.g., Hamilton, 2011), while other field observations and geodynamic modeling support that subduction may have already appeared in the Archean (Moyen & van Hunen, 2012; Nutman et al., 2009). These tectonic models may be acompanied by dissimilar crustal formation and deformation processes (Cagnard et al., 2011; Fischer & Gerya, 2016; Sizova et al., 2014), which may result in significant tectonic imprints in the crust that can be readily detected geophysically (e.g., Abbott et al., 2013; Clowes et al., 1998; Jones, 2013; Kennett & Saygin, 2015; Snelson et al., 1998; Thompson et al., 2010; Thybo & Artemieva, 2013; Yuan, 2015).

The velocity of seismic waves is a frequently used parameter to study tectonic processes associated with crustal growth and evolution. In the middle and lower crust where direct samples are unavailable, seismic velocity offers an indirect way to infer the composition and physical state of the continental crust (Christensen & Mooney, 1995; Rudnick & Gao, 2003). High-resolution seismic velocity images help better constrain crustal architecture and can add significant complementary information to advance our understanding of crust formation and evolution processes (Christensen & Mooney, 1995; Rudnick, 1995; Rudnick & Fountain, 1995; Rudnick & Gao, 2003). For example, slow crustal seismic velocities observed in several Archean cratons (Abbott et al., 2013; Christensen & Mooney, 1995) are associated with a felsic bulk crustal composition; this
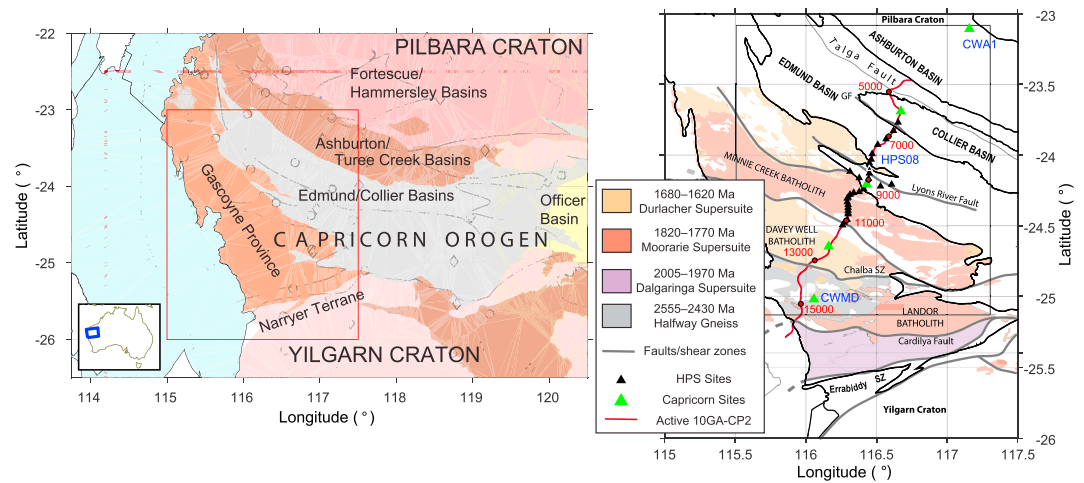
Figure 1. (a) Tectonic setting of the Paleoproterozoic Capricorn Orogen in the West Australian Craton and (b) a close view of the Glenburgh Terrane (modified from Korhonen & Johnson, 2015), as indicated by the red rectangle in a. Features in b include the passive-source seismic array (black and green triangles for HPS and COPA, respectively) and the active-source transect 10GA-CP2 (thin red line). Numbers along the active-source line show the common depth point (CDP) locations discussed in the text. Major faults (gray lines) are marked. Black contours are the terrane structural boundaries. Color coded in (b) are the regions affected by the major tectonothermal events during the cratonization.

compares to more mafic lithologies commonly found in the post-Archean crust (e.g., Rudnick & Gao, 2003; Tang et al., 2016) and favors a transition in crust formation processes that may reflect secular cooling of the Earth (e.g., Abbott et al., 2013; Johnson et al., 2014; Yuan, 2015).

In this study, we are interested in a late-Archean to Paleoproterozoic crust in the Capricorn Orogen of the West Australian Craton (WAC; Figure 1). The core region of the orogen, the Glenburgh Terrane, is interpreted as an exotic crustal fragment, compared with the neighboring Archean Pilbara and Yilgarn Cratons. The basement rocks were first formed ~2,600 Ma, with inherited zircons dated at nearly 3,500 Ma (Johnson et al., 2011, 2017). The orogen played an important role in assembling the WAC through two stages of Paleoproterozoic Orogenies (2215–2145 Ophthalmia and 2005–1950 Glenburgh Orogenies; Johnson et al., 2011) and experienced episodes of intracratonic thermal events in over a billion years of the cratonization processes (see a summary in Johnson et al., 2017; also see section 2). The region therefore affords a unique opportunity to associate crustal seismic structure to the crust formation and evolution processes in this prolonged tectonic history.

We constructed a crustal shear wave velocity model beneath a high-density temporary deployment that straddles the north boundary of the Glenburgh Terrane (Figure 1b). Our goal was twofold: we first explored the feasibility and benefits of obtaining a probabilistic high-resolution crustal shear wave velocity model by combining array dispersion measurements with a regional background velocity model that contains Moho topography; then we showed in detail how the new crustal velocity model can help to obtain an improved image of the crustal architecture, which, as illustrated in our recent multiple-disciplinary researches (Dentith et al., 2018; Yuan et al., 2017) can lead to new understandings regarding the regional tectonic processes. Our results show that the modified inversion technique can provide crustal velocity models with robust details. The new velocity model not only compares favorably with other crustal models but also adds complementary information (crustal velocity) that is able to better constrain the Precambrian crustal tectonics in the region.

2. Tectonic Setting

The Capricorn Orogen (Figure 1) is an ~1,000-km long by ~500-km wide region of deformed metaigneous and metasedimentary rocks between the Archean Pilbara and Yilgarn Cratons (Cawood & Tyler, 2004) in central Western Australia. The orogen recorded the punctuated Paleoproterozoic assembly of these cratons, and an exotic continental fragment, the Glenburgh Terrane, to form the West Australian Craton (WAC): the assembly of the WAC started when the Glenburgh Terrane collided with the Pilbara Craton during the 2215–2145-Ma Ophthalmia Orogeny (Johnson et al., 2011; Occhipinti et al., 2004), and subsequent collision

of this combined terrane with the Yilgarn Craton took place during the 2005–1950 Ma Glenburgh Orogeny (Johnson et al., 2011). The subduction of oceanic crust during the 2005–1950 Ma Glenburgh Orogeny is well documented in the southern margin (e.g., see Johnson et al., 2011), but no magmatic arc associated with the earlier 2215–2145 Ma Ophthalmia Orogeny is currently identified in the north. Following the assembly of the WAC, the orogen was structurally and thermally reworked during a series of punctuated, intraplate orogenic events over a period of more than one billion years (Johnson et al., 2011, 2013; Sheppard et al., 2004, 2010).

Our study region, the Glenburgh Terrane, part of the Gascoyne Province, is the oldest component of the Capricorn Orogen (Figure 1). Isotope studies (Johnson et al., 2011, 2017) show that four major cycles of magmatism are well recorded in the Province crust (Figure 1b): (1) the 2555 and 2430 Ma granite gneisses of the Halfway Gneiss. The inherited zircons in the Halfway Gneiss suggest that the oldest basement rock, although not directly exposed, may have formed sometime between 3500 and 2800 Ma (Johnson et al., 2011); (2) the 2005–1975 Ma Dalgaringa Supersuite, formed in the 1965–1950 Ma Glenburgh Orogeny during the collision of the Pilbara Craton-Glenburgh Terrane with the Yilgarn Craton took place; (3) the Moorarie Supersuite and (4) the Duriacher Supersuite, which are associated with the 1820–1770 Capricorn and 1680–1620 Ma Mangarroon Orogenies, respectively. The granitic magmas generated during these two cycles show a progressive enrichment in heat-producing elements (Korhonen & Johnson, 2015), suggesting a progressive fractionation of the terrane crust since the assembly of the WAC. The Gascoyne Province therefore preserves a prolonged history of terrane formation, early subduction/craton assembly, and intracratonic crustal reworking and differentiation that led to the WAC stabilization, and renders itself an ideal candidate for whole-crust geophysical imaging and association with the various early crustal origin and evolution processes.

Major crustal structures of the Capricorn Orogen are inferred from magnetotelluric, gravity, and seismic studies (Aitken et al., 2013; Alghamdi et al., 2017; Dentith et al., 2018; Heinson et al., 2011; Reading et al., 2012; Selway et al., 2009). In particular, based on significant differences in reflection character, a deep seismic reflection survey (Johnson et al., 2013) located several major crustal blocks, which are separated by several south dipping fault zones that can be traced to major suture zones on the surface. Numerous upper crustal reflectors were imaged that spatially coincide with volumetric Proterozoic granite batholiths in the region. Johnson et al. (2013) suggested that punctuated reworking of the craton is responsible for the crustal architecture. Recent geophysical studies add significant information regarding the crustal architecture and associated tectonic processes (Alghamdi et al., 2017; Dentith et al., 2018; Murdie et al, 2016; Pina-Varas and Dentith, 2017; Yuan et al., 2017). Receiver function analyses (Dentith et al., 2018; Yuan et al., 2017) revealed a systematic variation in the Vp/Vs ratios across the major suture zones, favoring different composition of the crustal domains. In this study, we contribute an absolute shear wave velocity model to the regional crust study by using ambient noise measurements and a Bayesian transdimensional approach, which are further discussed below. We show how this model can contribute to better understanding of the structure and evolution of the crust in this region.

3. The High-Density Passive-Source Array and the Ambient Noise Measurements

The dispersion data came from a year-long High-density Passive Source (HPS) transect, which was deployed from October 2014 to October 2015 (Figure 1). The HPS array is a subarray of the ongoing Capricorn Orogen Passive-Source Array (COPA; Gessner et al., 2015) and was designed to straddle the northern Glenburgh Terrane boundary and to purposely follow the existing reflection line 10GA-CP2 and the colocated magnetotelluric survey (Heinson et al., 2011; Selway et al., 2009). The array was composed of 25 Trillium Compact (PV120-SV1, 120-s to 100-Hz) sensors. Station spacing varies from 2 km in the southern half of the array in the Glenburgh Terrane to 4 km across the terrane boundary and 8 km in the Proterozoic Edmund Basin further to the north. Five broadband (Guralp 30s 40T and ESPC sensors) stations of the COPA deployment are also included in the analysis to extend the lateral coverage over 200 km. Waveforms were recorded at 100-Hz sample rate using battery-operated 24-bit data loggers designed and manufactured by the Australian National University. During the last 3 months of the experiment, four stations were relocated to the middle of the transect along the strike of the terrane boundary. In the 1 year deployment period the array achieved 70% data recovery with data loss due to drained battery toward the end of each 3-month recording period (Table S1 in the supporting information).

To extract short-period dispersion measurements, we followed the approach of Stachnik et al. (2008), in which the crustal and lithospheric velocity structure beneath the Yellowstone hot pot track was studied.
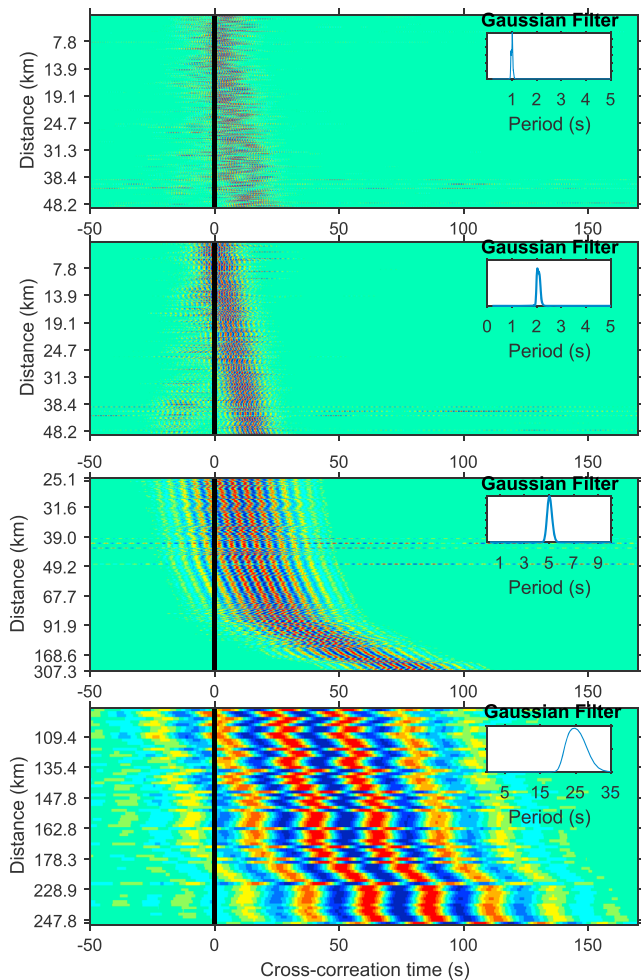
Figure 2. Stacked cross-correlation waveforms showing coherent dispersion signal from 1 s (top panel) to 25 s (bottom panel). The waveforms are sorted by path length in distance (*y* axis of plot). Inset in each panel shows the Gaussian filter applied to the waveforms.

The waveforms were first downsampled to 10 samples per second (sps) rate and were cut into 12-min long, 10% overlapping waveforms, which were further demeaned and detrended. Simultaneous recordings among all possible station pairs were cross correlated and amplitude normalized. For each station pair, anomalous traces with RMS amplitude greater than twice the standard deviation were removed, and a bootstrap resampling (Efron & Tibshitani, 1986) was used to generate 100 sets of data. Each of these bootstrapped data sets was then linearly stacked and averaged to form the final cross-correlation function. During this step, several stations with GPS timing problems were recognized (Figure S1), and time corrections were found by applying a cross-correlation technique (VanDecar & Crosson, 1990) to the waveforms in the negative and positive time ranges of daily stacks. The data were corrected accordingly before forming the final cross-correlation function (Table S2). The bootstrapping procedure takes advantage of stacking a large number of traces (average ~18,000 per station pair) that effectively stack up the signal-to-noise ratio and empirically removes the effects of large amplitudes from earthquake sources and the bias due to temporal variations in the noise sources (Stachnik et al., 2008). Group velocity measurements were determined using the Automatic Frequency Time Analysis code (Bensen et al., 2008; Levshin et al., 1972).

Figures 2, 3 show data examples and the related dispersion measurements. Coherent signals are prominent in the stacked waveforms (Figure 2) throughout the period range of our interest (1 to 30 s), with more measurements in the range below 10-s period (Figure 3a). Figure 3b shows the average dispersion measurements across the array. The group velocities are, in general, fast (~3.2 km/s; Figure 3b) in periods that are sensitive to the upper and middle crusts, consistent with the values found in Western Australia in previous continental-scale ambient noise studies (Saygin & Kennett, 2010, 2012). Figure 3c shows the group velocities for three paths that sample different regions of the crust (stations shown in Figure 1). Note that across the terrane boundary different patterns are found in the observed group velocities: within the terrane (blue) the velocity is fast at short periods (<15 s) with the peak around 8 s and decreases quickly after 15 s. The pattern is opposite outside the terrane (red), and the low velocities at short periods correspond spatially to the Edmund/Collier Basins at the surface.

4. Group Velocity Inversion and Resolution Test

The measured group velocities were inverted for group velocity maps in a 2-D region centered on the array. The inversion algorithm is the fast-marching surface wave tomography package (Rawlinson & Sambridge, 2005). Given that the HPS array is essentially a line array, the 2-D region is defined as 310 km in latitude and 205 km in longitude with 50 and 10 grid points, respectively, focusing more on the structure along the transect. For each period, the mean group velocity was used as the starting model. The damping parameters and the number of nonlinear iterations were decided empirically using the elbow of an *L*-curve between the model RMS value and the misfit RMS value (Menke, 1989). Figure S2 shows an example of choosing the optimal damping parameter and number of iterations for the inversion for 7-s period.

The inverted group velocities are presented in Figure 4, interpolated along the crooked active source 10GA-CP2 line (Figure 1b). We chose to present our results along the 10GA-CP2 transect to directly compare the velocity model with other crustal models that are interpreted along the line in the active-source (Johnson et al., 2013), receiver function and reprocessed magnetotelluric models (Dentith et al., 2018; Piña-Varas & Dentith, 2017). A strong lateral variation in the group velocities is present, but, in general, the pattern in the inverted group velocities confirms that seen in the raw dispersion data; the southern portion of the array
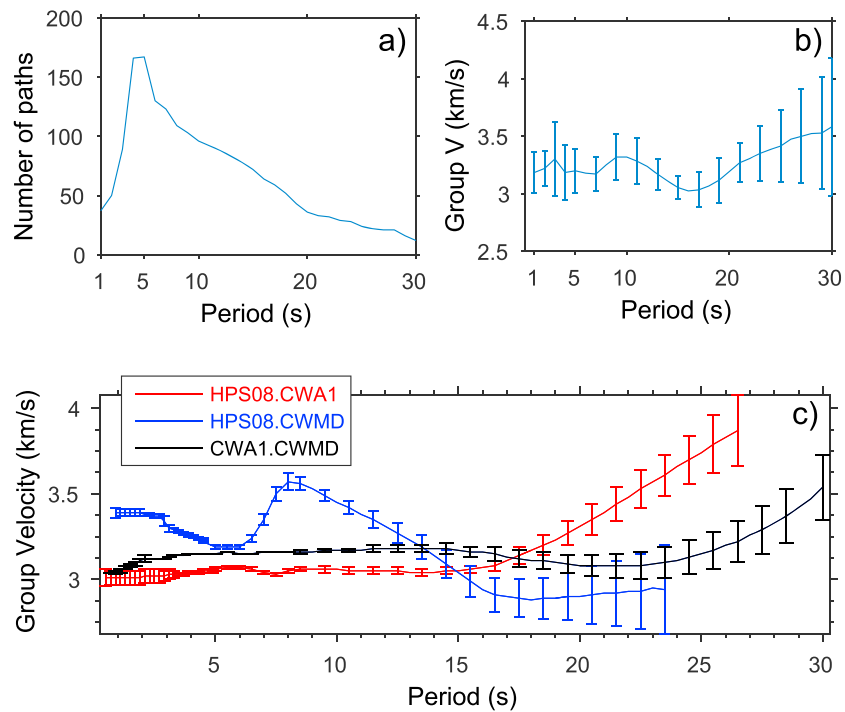
Figure 3. Example of dispersion measurements. (a) The total number of measurements for the frequent frequency range (1–30 s) used in this study. (b) The average group velocity with errors for all paths. The errors are approximated using bootstrap. (c) Dispersion measurements for three paths outside the Glenburgh Terrane (red), in the Terrane (blue), and along the whole transect (black), respectively. Stations are marked in Figure 1.

(e.g., > CDP (common depth point) Location 9000; see Figure 1 for location) is, in general, faster at the short periods (up to 12 s; corresponding to the shallow-to-middle crustal depth). This shallow crust high-velocity feature extends north to the boundary between the Glenburgh Terrane and the Proterozoic Edmund Basin (<CDP Location 7400). Beneath the high-velocity upper crust, a low-velocity region is present in the 12 to 20-s period range (middle crust) throughout the Glenburgh Terrane. North of the terrane boundary, in the Proterozoic Edmund and Collier Basins, the group velocities are slow up to nearly 20 s (upper to middle crust) and are fast in the 20 to 30-s period range (toward the lower crust).

To assess the resolving power of the dispersion data set, a simple synthetic model was generated, which is composed of bands of alternating fast (4.05 km/s) and slow (2.45 km/s) velocities (Figure 5). Depending on individual station paths, the width of the velocity bands varies from 12 km beneath the HPS array stations to over 48 km near the COPA stations outside the HPS array. For each period, synthetic traveltimes were computed using the paths of the real data and then inverted with the same damping used for real data. The
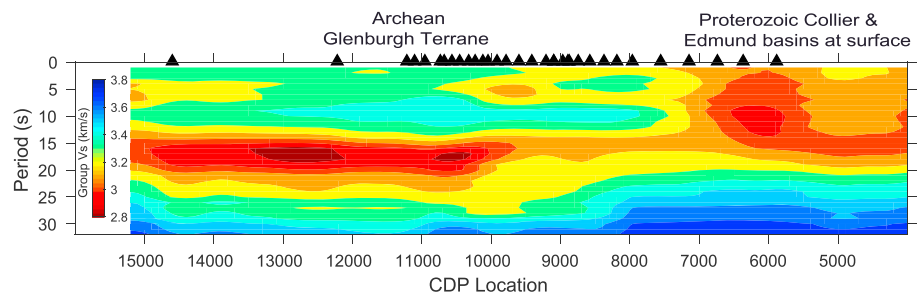

Figure 4. Group velocity inversion results plotted for all periods along the active-source 10GA-CP2 transect. Black triangles show the station locations.
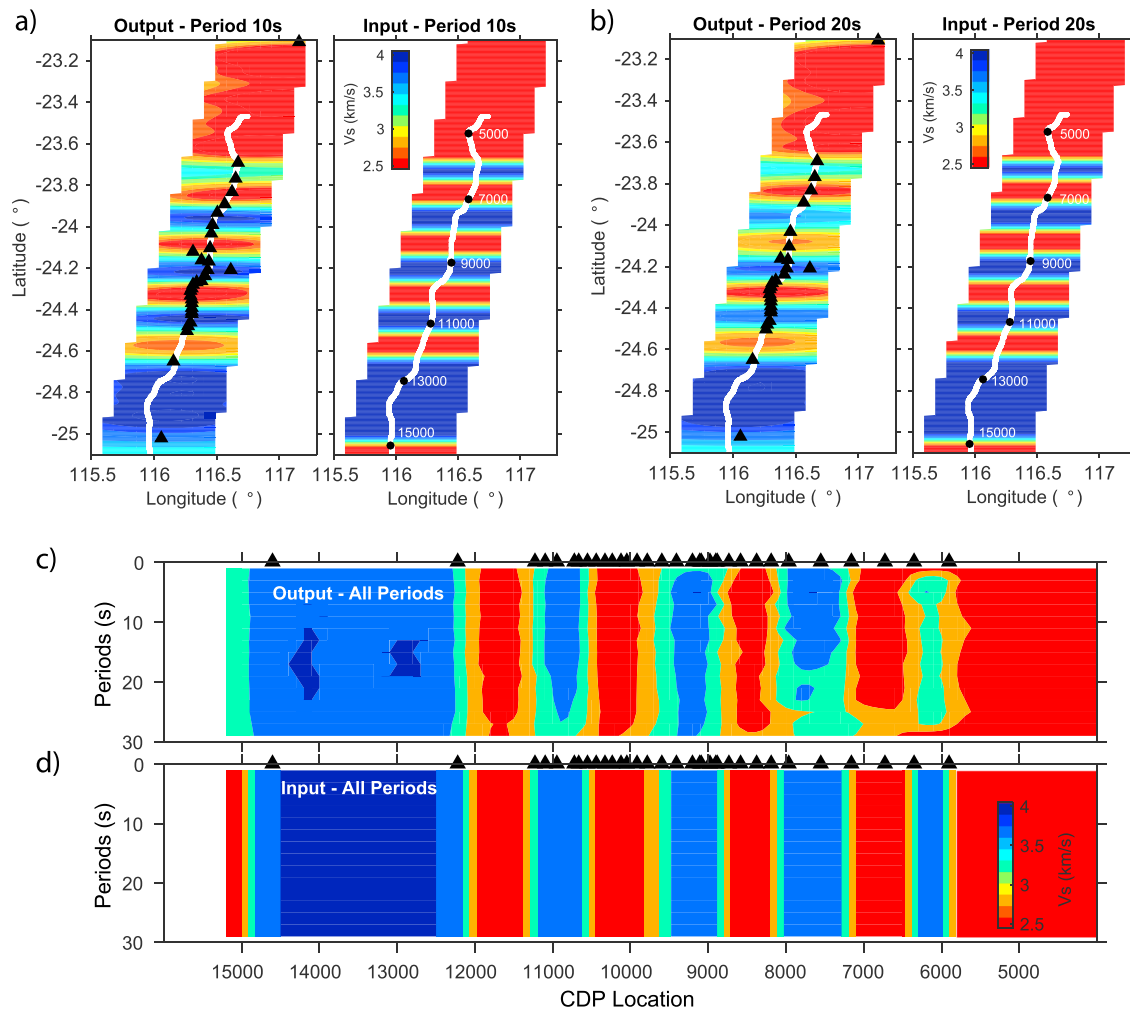
Figure 5. Resolution tests for the group velocity inversions. (a) The output (left) and input (right) models for the10-s group velocity inversion. Black triangles show the stations. Black dots show the CDP locations along the 10GA-CP2 line. (b) Same as (a) but for the 20-s inversion. (c) A cross-section-like plot showing the recovered velocity model, by combining all periods along the active-source profile. (d) The input model associated with (c).

inversion converged quickly after three iterations. Figures 5a and 5b show two map views of the recovered model and the input model at 10 and 20 s, respectively. Figure 5c shows the recovered models combined for all periods and plotted along the 10GA-CP2 transect. Compared with the input model (Figure 5d), the inverted model shows various amount of amplitude recovery (70% to 90%, in general, but smaller near the edges of the model); on the other hand, the overall recovery of the banded structural pattern beneath our array is very good.

5. Transdimensional Inversion of Dispersion Curves With A Piori Constraints

A commonly used method to obtain a crustal velocity model is to jointly invert receiver function waveforms with surface wave dispersion measurements (e.g., Bodin, Sambridge, Tkal, et al., 2012; Du & Foulger, 1999; Julia et al., 2000). The combination of these two data types offers tighter constraints to both the depth of discontinuities and volumetric velocity heterogeneities. However, since the sensitivity of receiver functions is confined to a cone-shaped zone beneath receivers, this technique is currently limited to the case where the inverted models are 1-D depth profiles beneath individual seismic stations. To obtain a spatially continuous 2-D or 3-D velocity volume, inverted 1-D depth profiles are usually laterally interpolated (e.g., Gilligan et al., 2014). Alternatively, receiver functions are interpolated between stations to form continuous receiver function gathers so that a joint inversion scheme may be applied (e.g., Deng et al., 2015).
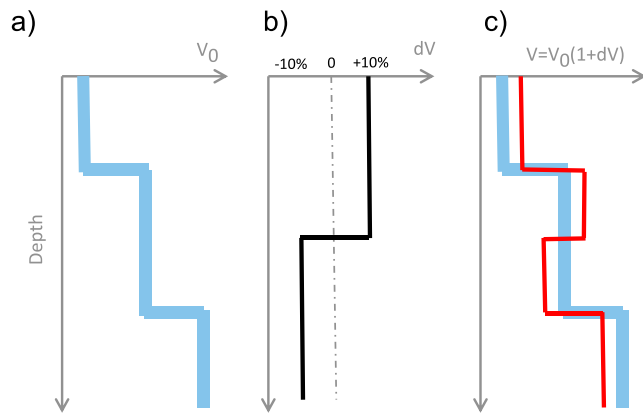
Figure 6. Illustration of the model parameterization: (a) layered reference model $V_0(z)$ that remains fixed during the inversion. (b) Model of velocity variations dV (z) defined by a number of layers, whose number, thickness, and value are variable and unknown in the inversion; (c) final model $V = V_0$ (1 + dV), simply constructed by adding the perturbations to the background model. Note that new discontinuities may emerge, which are determined by the data.

In this work, instead of performing a joint inversion at each station, we implemented a modified transdimensional Bayesian inversion technique (Bodin, Sambridge, Rawlinson, et al., 2012; Bodin, Sambridge, Tkal, et al., 2012; Bodin et al., 2014) to combine information from dispersion curves (group velocities in Figure 4) with a reference velocity model that contains a smoothly varying 3-D crustal velocity model and Moho topography. At each geographical location, we carry out a 1-D inversion of the local dispersion curve and invert for a perturbation around the reference model that contains a Moho. The set of 1-D inverted models obtained at each location can then be combined to produce a laterally varying crustal model that preserves the topography of the Moho contained in the reference model.

This approach differs from previous transdimensional inversions that used only dispersion data (e.g., Pilia et al., 2015; Young et al., 2013), where the reference model was set to a homogeneous half-space with no discontinuities, and the a priori distribution for velocity variations was set to a uniform distribution with relatively wide but physically plausible bounds. Here the goal is different, as we wanted to include some available information that is not directly contained in our dispersion data, for example, a laterally varying smooth crustal velocity model and Moho topography. The Australian Seismological Reference Model (AuSREM; Kennett et al., 2013; Salmon et al., 2013) provides a reasonable representation of such crustal velocity and Moho variations that are spatially continuous throughout our study region. The AuSREM crustal velocity model is built from five-layer representations of refraction and receiver function studies and ambient noise tomographic information and produces a representative model that captures the major features of the continental structure (Salmon et al., 2013).

5.1. Inverting Velocity Perturbations Around a Reference Model

For each geographical location, our unknown 1-D seismic model V (z) is parameterized in terms of perturbations dV (z) around a reference model $V_0(z)$

$$V(z) = V_0(z)(1 + dV(z)) \tag{1}$$

where the reference model $V_0(z)$ is defined as a stack of constant velocity layers (see Figure 6). This background model allows us to impose discontinuities that may not be resolved by dispersion data and that will remain fixed during the inversion (e.g., the Moho). The perturbation model dV (z) is unknown in the problem. Note that these perturbations do not need to be small, as there is no linearization involved in the inversion. This may lead to new intracrustal velocity variations that are not present in the reference model but required by the ambient noise dispersion data. The perturbation model dV (z) is also defined as a stack of layers with constant value, and the number of layers, their value, and their thickness are all free parameters to be determined by the data.

We formulate the inverse problem in a Bayesian framework where all information is represented in probabilistic terms. The solution of the problem is the posteriori probability distribution, which represents the probability density of the model parameters $\boldsymbol{m}$ describing V (z), given the observed dispersion curve $\boldsymbol{d}$, and given our choice for $V_0(z)$. Bayes' theorem is used to combine prior information on the model with the observed data $\boldsymbol{d}$ to give the posterior probability density function:

$$\text{posterior} = \text{likelihood} \times \text{prior}$$
$$p(m|\, d) = p(d\,|\,m)\,p(m) \tag{2}$$

The term p ($\boldsymbol{d}|\boldsymbol{m}$) is the likelihood function, which is the probability of observing the measured data given a particular model $\boldsymbol{m}$. The likelihood depends on the mathematical model used for data noise and is maximum when the estimated data for model $\boldsymbol{m}$ equal the observed data $\boldsymbol{d}$. p ($\boldsymbol{m}$) is the a priori probability density of $\boldsymbol{m}$ and represents what we know about the model $\boldsymbol{m}$ before measuring the data. Hence, the posterior
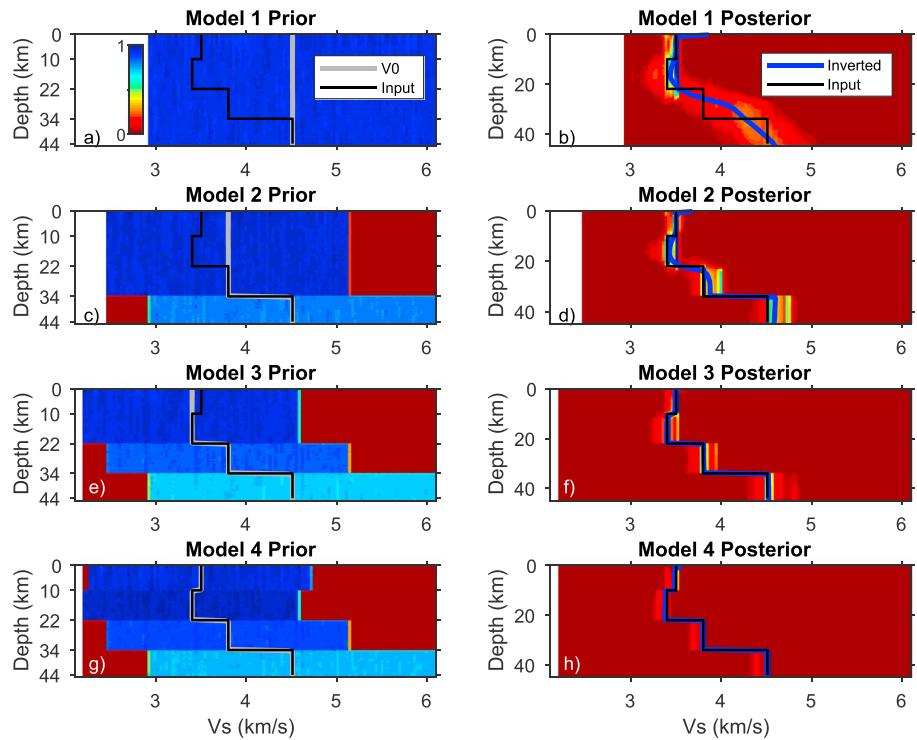
Figure 7. Synthetic tests for the simple model that has a three-layer crust over the half-space. The left panels (a, c, e, and g) are for the four reference models, showing the prior probability distribution (color background), the input model (thin black lines), and the reference models V_0 (thick gray lines). The right panels (b, d, f, and h) show the posterior density distribution and the posterior mean (inverted; thick blue lines) models. The input model (thin black lines) is also plotted for comparison.

distribution represents how our prior knowledge of the model parameters is updated by the data. If the prior and the posterior distributions are the same, then the data add no new information.

The reversible-jump Monte Carlo algorithm (Green, 1995) is used to generate samples from the posterior distribution, that is, an ensemble of vectors $dV(z)$ whose density reflects that of the posterior distribution. A random walk explores the model space with three different types of perturbations for $dV(z)$: (1) changing the depth of a discontinuity in dV, (2) adding or removing a layer in dV, and (3) changing the value of a layer in dV. The estimated level of data noise is also a free parameter that is perturbed along the random walk. At each step of the random walk, a new model $dV(z)$ is proposed and data are estimated for the model $V = V_0$ $(1 + dV)$. The estimated dispersion curve is compared to observations, and the likelihood of the proposed model is computed. The proposed model is either accepted or rejected in the ensemble solution. After a large number of iterations, the ensemble of accepted models can be used to approximate the posterior distribution.

The complexity of the model $dV(z)$, i.e., number of layers and the level of data noise are left as unknown parameters in the inversion (transdimensional, i.e., where the dimension of the parameter space is a variable to be solved for; Sambridge et al., 2006). Because the algorithm prevents overfitting the data, it penalizes overcomplex solution models (Bodin, Sambridge, Rawlinson, et al., 2012). In addition, uncertainties in the solution and trade-offs between model parameters can be evaluated using the posterior model variance and covariance. For a detailed description of the model parameterization and the algorithm, we refer the reader to Bodin, Sambridge, Tkal, et al. (2012).

5.2. Synthetic Models and Tests

Two sets of synthetic tests were considered to illustrate the resolving power of the modified technique. In Figure 7, a three-layer crustal model with a low-velocity midcrustal layer was constructed on top of a half-space (thin black line). The group velocities were computed to 30 s using the DISPER80 package (Saito, 1988), which utilizes the technique of normal mode summation in a spherical Earth with Runge-Kutta matrix

integration (Takeuchi & Saito, 1972). Random Gaussian noise (RMS 0.1 km/s) was added to this synthetic data set. Four reference models (V_0; thick gray lines in Figure 7) were considered: Model 1, a simple homogenous half-space; Model 2, a constant velocity crust over a half-space mantle; Model 3, same as Model 2 but with a lower crustal layer (Model 3); and Model 4, where the reference model equals the input model in black.

Note that the transdimensional inversion allows the velocity to vary up to 35% at all depths down to 120 km around the reference model V_0. That is, for each layer that defines the model $dV(z)$, the value of the perturbation model can vary within the range $[-0.35 + 0.35]$ of V_0. This can be seen by looking at the prior probability distribution in the left panels in Figure 7. The color density plot represents the 2-D histogram for a large ensemble of random models $V(z)$ distributed according to the prior. This ensemble of models is obtained by simply running our inversion code but by setting the likelihood to 1 in equation (2), so the reversible jump algorithm samples the uniform prior distribution. This density plot is convenient to visualize the ensemble solution, and it is particularly useful to demonstrate the constraints that are imposed a priori on Vs. As expected, velocity values at each depth are distributed uniformly around the reference model $V_0(z$; thick gray lines).

The result of a Bayesian inversion is the posterior distribution drawn from an ensemble of 500,000 models, plotted here in the right panels (Models 1–4 posterior; b, d, f, and h in Figure 7). In Bayesian inference, the posterior is meaningful only in its comparison to the prior. By comparing our posterior ensemble of models (right panels) to the prior ensemble (left panels), the differences that are due to the data are clearly shown. The posterior mean model (thick blue lines) is simply constructed by taking the average velocity at each depth across the ensemble posterior solution. This model is the "average solution." Note here that besides the average solution, other statistical moments of the distribution can be used for interpretation (e.g., the median, maximum). As shown below in section 5.3, the standard deviation can be used to depict the level of uncertainty around the mean. When models $dV(z)$ with different transition locations are averaged, the sharp changes present in individual models $dV(z)$ are smoothed out in the average solution. Given the sensitivity of surface wave measurements, some discontinuities in the true model (thin black lines) are usually not fully resolved, and the average solution is only a smooth version of the true model. This is clearly shown for Model 1. However, when discontinuities (crustal layers) are included in the reference model (Models 2 to 4), the inversions better recover the structure in the crust, and the posterior distributions are substantially tightened.

In real data inversions, however, it may be difficult to find adequate prior models for the crust. The real crust is far more complex, and both the crustal velocities and the Moho topography given in regional models may contain errors. To investigate in these cases to what extent different reference models may affect the inversion, another set of synthetic tests was considered (Figure 8). The input model (thin black lines) is a smoothly layered crustal model composed of a low-velocity layer in the upper crust (0–10 km), a high-velocity layer at 10–15-km depth, and a low-velocity layer underneath (>15 km to lower crust). These structures mimic the real data inversion results at CDP location 10000 near the center of the array, where the smooth velocity layers agree broadly with the corresponding velocity gradients seen in the receiver functions (see section 6). The Moho is at 38 km based on results from both the active source study (Johnson et al., 2013) and the receiver functions (Dentith et al., 2018). The synthetic data set was generated in the same manner as in the previous three-layer cases. Four reference models were tested (V_0; thick gray lines in the left panels): Model 1, a homogeneous half-space model (Vsv = 4.8 km/s); Model 2, a constant velocity crust (4.2 km/s above 38 km) over the half-space mantle (4.8 km/s); Model 3, a smoothly layered crust model, which is the average of the AuSREM crustal model along the 10GA-CP2 transect, with the Moho at 38 km and Vsv = 4.8 km in the half-space; and Model 4, the same as Model 3, but the Moho is set incorrectly to 43 km.

Note that the reference models do not contain the alternating velocity layers in the input model. This layering pattern is, however, recovered to a large extent in all inverted models (the posterior mean; thick blue lines in Figures 8b, 8d, 8f, and 8h). For Model 1 with the homogenous prior, the inverted model does not fully recover the velocity drop around 20-km depth, and a large-amplitude overshoot occurs both at the surface and beneath the Moho. For Model 2 in which a constant crustal velocity (4.2 km/s) is included in the reference model, the inverted model does not vary much compared with Model 1, but the velocity contrast across the Moho is significantly larger than both Model 1 and the input. (We also tested another velocity of 3.7 km/s for the whole crust; the large-velocity contrast across the Moho, however, remained.) Note that
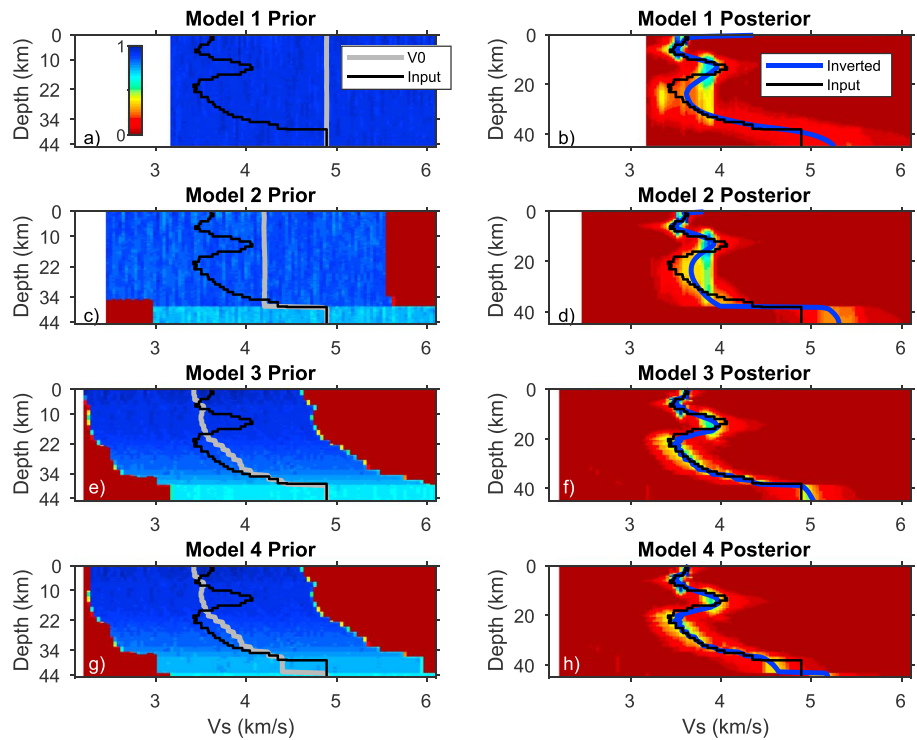
Figure 8. Synthetic tests for the model with smoothly layered crust. The left panels (a, c, e, and g) are for the four reference models, showing The prior probability distribution (color background), the input model (thin black lines), and the reference models (thick gray lines). The right panels (b, d, f, and h) show the posterior density distribution and the posterior mean (inverted; thick blue lines) models. The input model (thin black lines) is also plotted for comparison.

for the first two reference models, the posterior distributions in the middle to lower crust are broad and multimodal, and the posterior means (thick blue lines) do not always follow the posterior maxima. For Model 3, the inverted model recovers the high-velocity and the low-velocity crustal layers and the velocity jump across the Moho. The posterior distribution is significantly tightened, and both the mean and maximum values in the posterior distribution follow the input model. For Model 4 in which the Moho in the reference model is set to 43 km, the inversion pushes the velocity jump to 43 km accordingly. In this case, however, the crustal structure above 38 km (the Moho depth in the input model) remains rather similar to Model 3.

These synthetic tests suggest that within the period range we considered, structures in the shallow crust may be well recovered regardless of the choice of reference models. Although both a homogeneous and a constant velocity crust reference model allow us to recover the main structural patterns in the whole crust, some amplitude mismatches are expected, especially in the lower crust. The constant velocity crust reference model results in a larger (than the input) Moho velocity jump, leading to lower velocity in the lowermost crust. This is a concern raised in some early dispersion inversions (Julià et al., 2003; Stachnik et al., 2008). For the lower crust, a layered reference model can improve the recovery of both the structural patterns and amplitudes. The Moho, if incorrectly set in the reference model, may be recovered at the assigned depth. It is therefore important to include robust Moho estimates in the reference model, and caution must be taken when interpreting the structure near the Moho.

5.3. Inverting for Crustal Velocity Models Beneath the 10GA-CP2 Line

In inverting the group velocity in Figure 4, we considered three reference models (Figure S4). Model 1 is a homogenous half-space, as in previous transdimensional inversions (Pilia et al., 2015; Young et al., 2013); Models 2 uses the 1-D average of the AuSREM crustal velocity across 10GA-CP2 transect and includes the AuSREM Moho topography; Model 3 is the same as Model 2, except instead of using the transect average, at each location the velocity was extracted from the AuSREM model. The velocity beneath the Moho is set
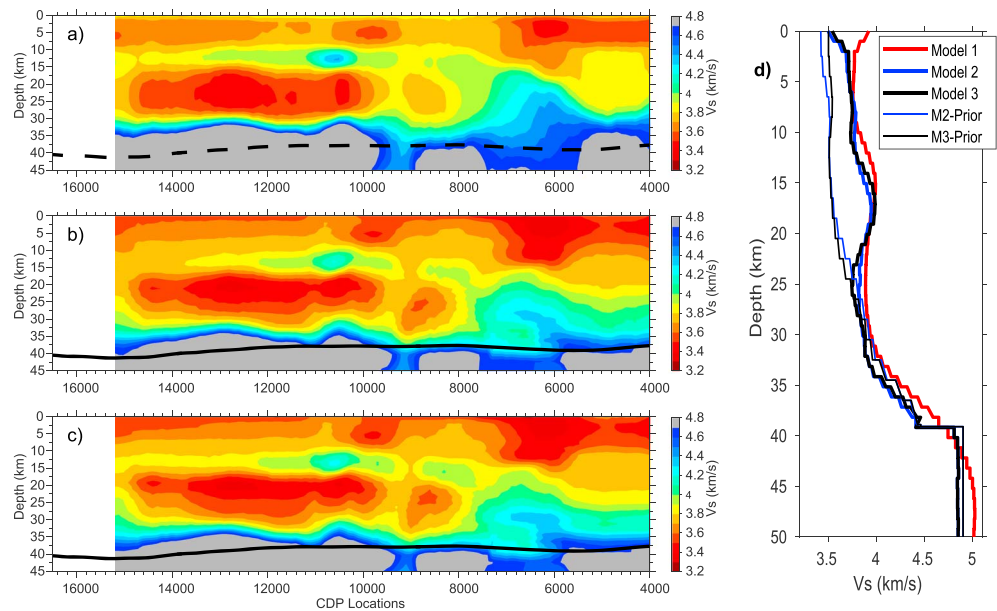
Figure 9. Inversion results using the three reference models discussed in the text. (a) Inversion using Model 1, a homogeneous model (i.e., where $V_0 = 4.89$ km/s for the half-space). (b) Inversion using Model 2, a 1-D background velocity model with Moho topography. The 1-D velocity model is the AuSREM crustal Vsv model averaged along the 10GA-CP2 transect. The Moho depth is extracted from the AuSREM models (Figure S4a). (c) Same as (b) but using Model 3, a 2-D background model with Moho topography. At each location a 1-D model is extraced from the AuSREM crustal Vsv model (Figure S4b). Black line in each panel shows the Moho. Note the Moho is only used in the reference Models 2 and 3. (d) The inverted 1-D velocity profiles at CDP location 8000; the two reference Models 2 and 3 are also plotted for comparison.

to 4.8 km/s throughout the transect. On a Cray Super computer (Magnus at the Pawsey Super Computing Centre, Western Australia), the inversion was performed using 576 independent Markov chains/CPUs that sampled the model space simultaneously and independently. Each chain was run for 30,000 models. The first 10,000 models of the chain (called the burn-in period) were discarded, after which the random walk was assumed to be stationary and models generated by the chain are asymptotically distributed according to the posterior probability distribution. At each location, the whole ensemble of models searched by the transdimensional inversion was averaged to give the 1-D posterior mean profile; 113 such 1-D profiles (from CDP Location 4000 to 15300) were combined to form a depth 2-D cross section, which can be compared with the available active source, magnetotelluric (MT) and receiver function results (see section 6). We also tested inversion using only 24 chains/CPUs (for the same number of 30,000 models per chain, but an inversion that was less explorative due to the smaller number of chains), which gave coarse-looking results but with similar structural pattern and velocity amplitudes; see Figure S5.

The three inverted velocity models are presented in Figure 9. One noteworthy observation is that the large-scale crustal structure remains systematically similar, despite the differences in the reference models (Figure S4). Between the homogenous background model (Model 1) and more complex models (Models 2 to 3), visible differences in both the velocity pattern and the amplitude are present in the middle to lower crust in the latter models. This is consistent with what we have observed in the synthetic tests (see more discussion below). Between Models 2 and 3, however, the structural differences seem minor. Figure S6 shows the spatial distributions of the number of velocity layers, a free parameter determined by the inversion. The three models have consistent patterns throughout the line, agreeing with the coherent large-scale crustal-scale features among the models (also see Table S3 for the inverted total number of layers for these models).

The three inverted models are evaluated using the BIC values (Akaike's Bayesian Information Criterion; Akaike, 1974) calculated from the total data misfit (Table S3) and the sum of number of layers determined by the inversion. For each model, the BIC values were computed as

$$\text{BIC\_all} = N \times \log\left(\frac{\text{misfit\_all}^2}{N\_\text{all}}\right) + k\_\text{all} \times \log(N\_\text{all}) \tag{3}$$
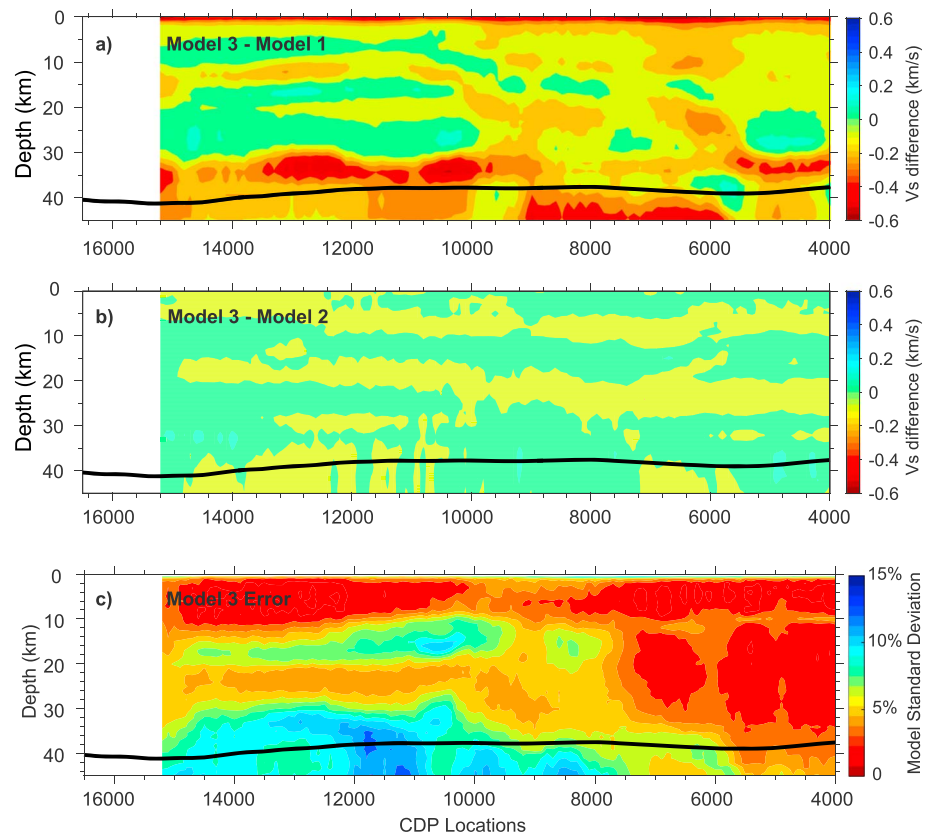
Figure 10. Differences in the inverted velocity structure introduced by layered reference models: (a) between the homogeneous half-space model (Model 1) and the final model (Model 3). (b) Difference between the 1-D and 2-D reference models (Model 2 and Model 3, respectively).

where the misfit value (misfit_all), number of parameters (k_all), and number of data (N_all) are simply the total sum of all locations where the 1-D velocity profiles were inverted. Table S3 suggests that Model 3 has the minimum BIC number and therefore is our preferred velocity model. Note that Model 3 also has the minimum total number of layers, suggesting that it is not necessarily more complex that the other two models.

The differences between the inverted models generated with the three reference models are further illustrated in Figure 10, where the final model (Model 3) is subtracted from the other models. The major differences introduced by the layered reference models are clearly present in the middle to lower crust, where our synthetic tests suggest better recovery of the structural pattern and the amplitude in similar cases. For example, between CDP locations 90000 and 15000, the high-velocity lower crust in Model 1 is pushed deeper toward the AuSREM Moho in Models 2 and 3; also, more structures are present at CDP locations ~6000 and 9000. Figure 10b shows that between Models 2 and 3, the inverted velocity models do not vary much, even though the smooth 2-D reference model varies up to ±4% in amplitude, and the lateral structural trend is nearly opposite to the inverted model (Figure S4b). The observations in Figure 10 suggest that adding prior crustal velocity constraints generally recovers more structural details in the crust model. This is consistent with other Bayesian Monte-Carlo inversions (e.g., Deng et al., 2015), which show that more detailed intracrustal structures emerge after incorporating prior velocity models. Figure 10c shows the standard deviation of the final model provided by the transdimensional inversion, plotted in percentage of Model 3. At most of the depth ranges the model error is well within 5% of the final model. Larger variations (~5 to 10%) occur south of CDP 8000, especially > CDP 10000, in both the lower crust and at depth ranges between 10 and 20 km.
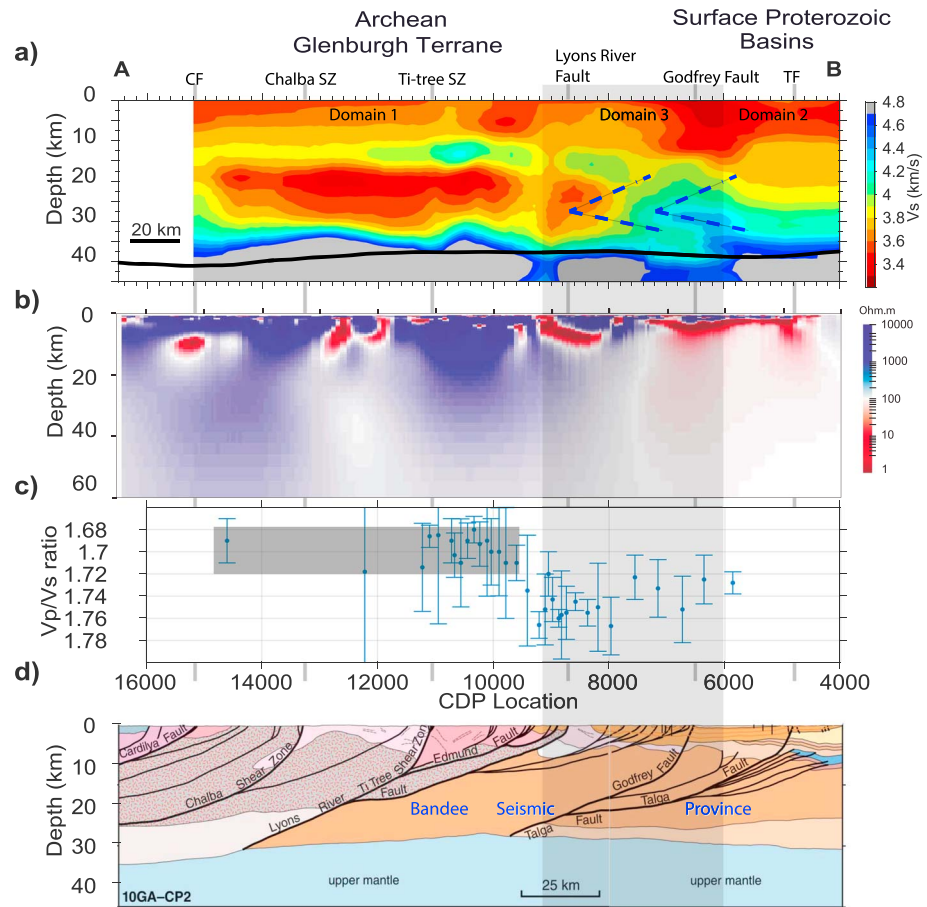
Figure 11. Crustal domains beneath the 10GA-CP2 transect. (a) The velocity model with annotated surface geological features. Faults and suture zones at surface are marked and indicated as vertical gray lines. Labels are the following: CF = Cardilya Fault; TF = Talga Fault; SZ = shear zone. The thick vertical gray bar shows Domain 3, approximately the transition region between Domains 1 and 2. Blue dashed lines indicate the tectonic wedges inferred from the active source and receiver function results (further discussed in section 6.2). The black line is the Moho interface from the AuSREM model. (b) The magnetotelluric model (P. Piña-Varas, personal communication, 2018) along the transect. (c) Vp/Vs ratios and associated errors from the receiver function H-k technique (modified from Dentith et al., 2018). The gray-shaded region indicates the small Vp/Vs ratios (~1.70) in the Glenburgh Terrane. (d) The active-source model interpretation of Johnson et al. (2013).

6. Crustal Velocity Model and Tectonic Implications

In this section, we review the new information revealed by the inverted velocity model, compare the velocity features with the surface geological structure, and correlate the velocity model with available crustal models obtained in the active source, MT, and receiver function studies. We further draw inferences about the crust formation tectonics of the Glenburgh Terrane and its role in the assembly of the West Australian Craton.

6.1. Crustal Domains

Three velocity domains (Domains 1 to 3 in Figure 11a) are recognized in the crustal velocity model, based on their unique spatial pattern and the association with surface geological futures. Domain 1 is entirely in the Glenburgh Terrane, between CDP locations ~9000 and 15000. It has a "reversed" velocity layering pattern; that is, a high-velocity shallow crustal layer (~15 km) sits on top of the low-velocity middle to lower crust. Domain 2 corresponds to the Proterozoic Basins (<CDP Location 6000), where a "normal" velocity layering is found where the crust velocity increases with depth. Domain 3 loosely defines the transition region between Domains 1 and 2 (indicated by the vertical gray bar in Figures 11 and 12) and contains two major suture zones, the Lyons River and Godfrey Fault systems at the surface. These velocity domains are present in all inverted models (Figure 9), suggesting that they are robust features.
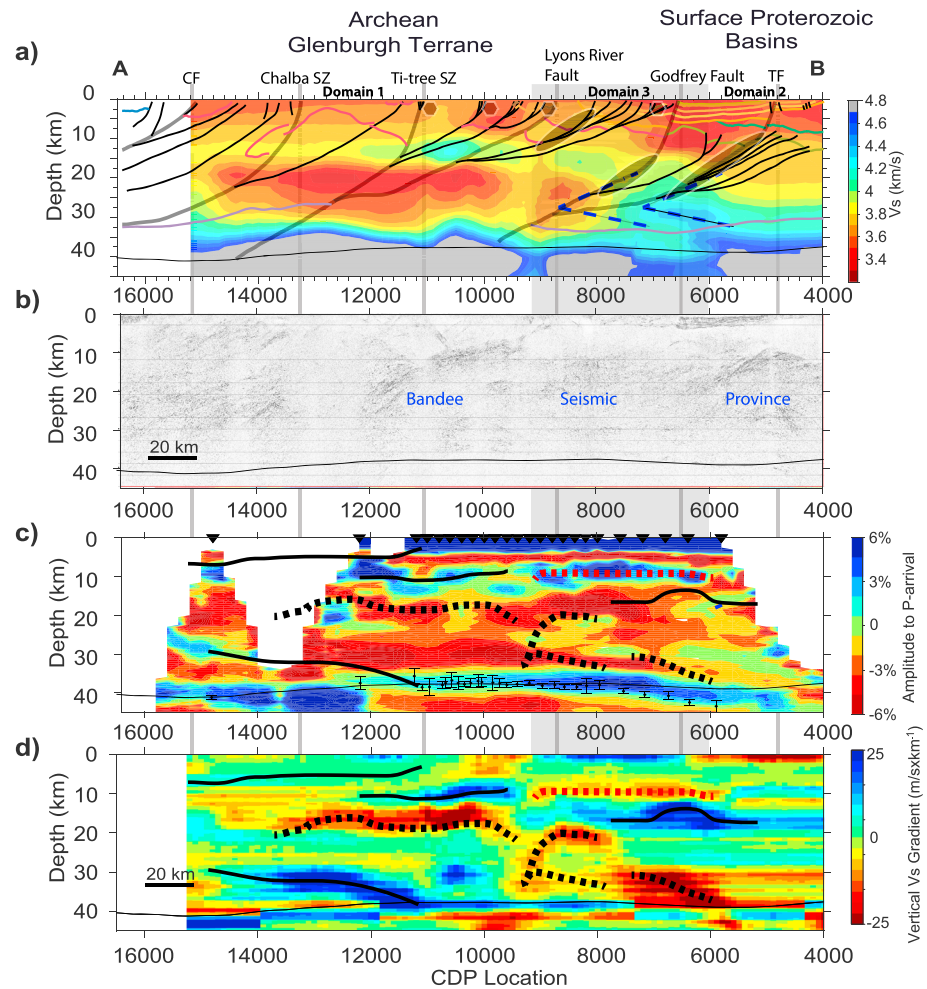
Figure 12. A comparison between the inverted shear wave velocity model and other seismic models. (a) The velocity model overprinted with the active source interpretation (Johnson et al., 2013). Features in the reflection interpretation include the following: thin gray and black lines, fault systems; red lines in the shallow crust, base of granite batholiths; and yellow and green lines, base of Proterozoic basins. Labels are the following: CF = Cardilya Fault; TF = Talga Fault; SZ = shear zone. (b) The migrated reflection model (Johnson et al., 2013). (c) Receiver function CCP image modified from Dentith et al. (2018). (d) Depth gradient of the inverted velocity model (d). The positive and negative depth gradients from the velocity model are approximated in solid and dashed lines in (c) and (d). Thin black line throughout the figure shows the Moho from the AuSREM model. Vertical bars in (c) are the Moho and the associated error estimated from receiver function H-k technique (Dentith et al., 2018).

The velocity domains correlate broadly with the spatial distribution of the crustal resistivity in the magneto-telluric model (Dentith et al., 2018; Piña-Varas & Dentith, 2017) and the Vp/Vs ratios (an indication of bulk crustal rock composition; Christensen, 1996) measured from the receiver functions. The MT model (Figure 11c) shows that in Domain 1 the crust is largely resistive, while in Domain 2 it is likely conductive (Pina-Varas & Dentith, 2017; Yuan et al., 2017). The receiver function model (Figure 11d) shows that Domain 1 has mainly low Vp/Vs ratios (~1.70), while elevated Vp/Vs ratios (1.72–1.75) are found in the transition region (Domain 3). North of CDP location 4000, a low Vp/Vs ratio (1.70) is measured at station CWA1 in the Pilbara Craton (see location in Figure 1b). The spatial coherence between the crustal domains in the velocity, resistivity, and the Vp/Vs ratios suggests that the surface geological structures, for example, the Glenburgh Terrane and the surface Proterozoic basins, represent deep-seated whole-crust domains, which possess different crustal composition, as may be inferred from the different bulk crustal properties and velocities (Christensen, 1996; Christensen & Mooney, 1995; Jones, 1992).

6.2. Comparison With Reflection and Receiver Function Models

In Figure 12, we compare the inverted velocity model with the active-source reflection and receiver function Common-Conversion-Point (CCP) models. These models sample the same crust along the 10GA-CA2 transect but are sensitive to different crustal properties, that is, the volumetric velocity variations (Figure 12a) and velocity contrast (Figures 12b and 12c). Along the transect, the reflection image reveals several steeply dipping features, which were interpreted as crustal scale faults (gray and black lines). In the crust, there seems to be a certain degree of spatial correlation between the inferred faults and the lateral variation in the velocity model (shaded dark regions in Figure 12a): for example, the Talga fault (TF), from 10 to 30 km depth in Domain 3; the Godfrey Fault, 15–25 km, in Domain 2; multiple locations in the Lyons River fault system, 5–20 km, in Domains 3 and 1; and likely the Ti-tree Shear Zone, <10 km, in Domain 1. Large discrepancies are also present, but mostly noticeable in the middle to lower crust in Domain 1, where the reflection profile draws a steeply south dipping Lyons River Fault. In the reflection interpretation, a large portion of the middle to lower crust beneath this fault is attributed as a "Bandee Seismic Province," which is interpreted as part of the Pilbara Craton. Given the continuous reversed layering velocity pattern, and the good resolution in this part of velocity model by the resolution tests (Figure 5), Dentith et al. (2018) argue that the deep crust here may still be part of the Glenburgh Terrane; see more discussion in section 6.3.

Vertical velocity gradients mapped in the receiver function CCP image (Figure 12c) are further compared with the depth gradients of the velocity model (Figure 12d). The spatial coherence is generally consistent in the whole crust: for example, in Domain 1, the positive gradients at 10–15 km, and between 30 and 40 km, as well as the negative gradient between 15 and 20 km; in Domain 2, the negative gradients between 20 and 35 km, surrounding the "wedge"-shape structure in the CCP image (further discussed in section 6.3; see also Dentith et al., 2018); and in Domain 3, the positive gradient at 15 km. In Domain 1, the positive velocity gradients at 10–15 km may be associated with many gently dipping reflectors (Figure 12b; see also interpreted Figure 11d), which are interpreted as the base of granitic batholiths revealed at the surface (Johnson et al., 2013, 2017; Korhonen & Johnson, 2015; also see Figure 1b). One large discrepancy is in the upper crust in Domain 2, where the receiver function shows a large positive gradient (slightly <10 km) but the depth gradient of the velocity model (slightly >10 km) is negative. We suspect the shallow basins, as seen in the reflection profile (yellow lines in Figures 12a and 12b; also see Johnson et al., 2013, for detail) may cause strong surface multiples that are falsely mapped to <10 km depth in the CCP image.

6.3. Redefining the Crustal Architecture and Possible Paleosubduction Signature

The northern boundary of the Glenburgh Terrane formed in response to the collision of the terrane with the Pilbara Craton during the 2.2-Ga Ophthalmia Orogeny (Johnson et al., 2011). Early studies combining surface geology, isotopes, magnetotelluric, and active-source imaging (Cawood & Tyler, 2004; Heinson et al., 2011; Johnson et al., 2013; Selway et al., 2009) draw the Lyons River Fault as the suture zone that separate the Glenburgh Terrane from the Pilbara crust. From the surface the fault system connects to a series of gently south dipping reflectors in the active source interpretation (Figure 11d). Based on the uniform reflectivity pattern and the change in the crustal resistivity (Heinson et al., 2011) that spatially extend into the lower crust in the Pilbara Craton, the middle to lower crust underneath the Lyons River Fault was interpreted as a domain of the Pilbara crust, termed the Bandee Seismic Province (Figure 11d; see also Figure 12b; Johnson et al., 2013). However, the reversed velocity layering pattern in Domain 1 and the resistive crust imaged in the MT model extend into Domain 3 to as far north as beneath the Godfrey Fault. Yuan et al. (2017) suggested that the crust of the Glenburgh Terrane may extrude beneath the Proterozoic basins (Yuan et al., 2017), although this portion of the crust in Domain 3 may have been deformed during the collisional processes. The leading edge of the Glenburgh Terrane may correlate at depth with the steeply south dipping fault structures marked by the high-velocity anomaly beneath the Godfrey Fault (Figures 11a, 11b, 12a, and 12c). See Dentith et al. (2018) for a detailed analysis of the crustal architecture in the region.

A puzzle associated with the Ophthalmia Orogeny is that no suprasubduction magmatic activity associated with this event is exposed on either the Pilbara Craton or the Glenburgh Terrane. Recent isotopic data from magmatic rocks that formed during subsequent intraplate orogenic events revealed the presence of an unexposed, deep-crustal reservoir with isotopic compositions and ages consistent with an Ophthalmian-aged magmatic arc (Johnson et al., 2017). Beneath the Godfrey Fault, the lower crust is present as a high-velocity feature (CDP Locations 8000 to 6000; see Yuan et al., 2017)). In many Precambrian collision zones, similar

high-velocity lower crust is regularly observed in active source studies (Thybo & Artemieva, 2013), which is attributed to mafic underplating associated with the syncollisional or postcollisional processes. Spatially associated with this high-velocity feature, both receiver functions and active source image show wedge-like dipping structures (marked in Figure 11a; see Figures 12a and 12c; also see Dentith et al., 2018; Yuan et al., 2017). Numerous seismic reflection sections have shown that such tectonic wedging may be required to accommodate horizontal deformation within accretionary orogens (Meissner, 1989; Snyder & Goleby, 2016). It is likely that the high velocity found in the lower crust may correspond to the mafic deep-crustal reservoir (Johnson et al., 2017) formed during the subduction leading the Ophthalmian orogeny; after solification, this high-velocity lower crust may have become dense and rheologically strong and therefore resulted in faulting along the edge to accommodate horizontal deformation during the terrane collision (Yuan et al., 2017).

6.4. Glenburgh Terrane: An Archean Microcontinent

In young orogens, low velocities imaged in the middle and lower crust are typically attributed to either loss of dense mafic lower crust due to lower crustal delamination (Beck & Zandt, 2002) or partial melts of aqueous or magmatic fluids due to thickening of the orogenic crust (e.g., Hammond & Humphreys, 2000; Hyndman & Shearer, 1989). In stable cratonic regions, low-velocity zones in the middle crust are also observed (e.g., Chen et al., 2015; Gu & Shen, 2015), which may result from recrystallization of granitic intrusions induced by syncollisional or postcollisional tectonothermal events associated with craton assembly (Chen et al., 2015). In the Glenburgh Terrane, a partial melt or fluid origin for the low-velocity middle to lower crust is, however, unlikely: the presence of melts or fluids would predict large Vp/Vs ratios (e.g., >2.0; Hammond et al., 2011), which is inconsistent with the terrane-wide low Vp/Vs ratio measurements (~1.70; Figure 11c). These seismic observations, on the other hand, favor an overall felsic granitic crustal composition (Christensen, 1996). Local isotope and structural geology studies suggested that the Glenburgh Terrane is a late-Archean-aged exotic terrane that is compositionally and structurally distinct from the neighboring Pilbara and Yilgarn Archean crustal provinces (Johnson et al., 2011; Occhipinti et al., 2004). The terrane-wide observations of low-velocity midcrust, low Vp/Vs ratios, and resistive crust further strengthen the argument that the Glenburgh Terrane is an Archean microcontinent.

We stress the Archean heritage of the inferred granitic crust, which may also be representative of several Archean crusts in a recent global compilation (Abbott et al., 2013). In the Capricorn Orogen, the first major tectonomagmatic event (see Figure 1b) was dated to the Neoarchean, and some of the proto crust may be even Eoarchean-aged (Johnson et al., 2011). The crust formation then may be likely cast in the Archean vertical accretion framework (e.g., Bédard, 2006), in which subsequent crustal differentiation and lower crust removal processes could lead to an overall felsic crustal composition (Abbott et al., 2013; Bédard, 2006; Johnson et al., 2014; Sizova et al., 2015; Yuan, 2015). The possible Paleoproterozoic subduction leading the 2.2-Ga Ophthalmian Orogeny (Johnson et al., 2011) is unlikely to be the major contributor of the felsic crust as proposed for other regions (e.g., Beck & Zandt, 2002; Chen et al., 2015; Chowdhury et al., 2017); instead, the subduction seems to affect the crust locally by leaving high-velocity mafic lower crust along the margin (Yuan et al., 2017). After the Ophthalmia Orogeny, isotropic signatures of the subsequent intracratonic magmatic events suggest that they are not mantle sourced (Johnson et al., 2017). Crustal remelting associated with these events may further contribute to the felsic crustal composition, by progressively fractionating the terrane crust and driving the heat-generating elements to shallow depth (Korhonen & Johnson, 2015), forming the terrane-wide granite batholiths at the surface (see Figure 1). The high-velocity shallow crustal layer may be associated with these younger magmatic events, possibly representing the accumulated residual solid during the formation of the volumetric batholiths (e.g., Johnson et al., 2013; Vanderhaeghe, 2009; Yuan et al., 2017).

7. Conclusions

Several interesting observations are noted in our exploration of the feasibility and benefits of the modified Bayesian transdimensional inversion in crustal structural imaging. The inversion is stable and robust: results obtained with different reference models show consistent large-scale features (e.g., the velocity domains). The inversion with a homogenous prior model provides a smooth version of the crustal velocity structure; with prior constraints such as a 1-D reference model and Moho topography, the inversions may improve the amplitude recovery and introduce some visible structural details in the deep crust. Comparisons show

that these structures are compatible with features in the higher-resolution crustal models. We conclude that it may be feasible to include a reference background velocity model, especially with Moho topography, as prior information in the transdimensional inversion. In this way, we have proposed here a method to combine in a consistent manner two different data types with different sensitivities to structures: (1) long-period seismic measurements (from surface waves) constraining volumetric velocity variations and (2) short-period observations (from receiver functions) constraining spatially continuous seismic discontinuities.

A high-resolution crustal shear wave velocity model was obtained along an ~200-km long cross section, which straddles the suture zone associated with the 2.2-Ga Ophthalmian Orogeny leading the assembly of the West Australian Craton. The crustal velocity model adds great detail to the crustal architecture and provides complementary information to support that the Glenburgh Terrane is a microcontinent originated in the Archean (Johnson et al., 2011; Yuan et al., 2017). The average low velocity favors a felsic or granitic composition of the Glenburgh Terrane, which was perturbed during intraplate thermal events in the stabilization of the West Australian Craton. As proposed in a series of recent geophysical studies (Dentith et al., 2018; Yuan et al., 2017) and highlighted in this paper, the distinct pattern in the velocity domains better delineates the northern margin of the Glenburgh Terrane. Compared with previous crust models, the terrane extends farther north and extrudes into the crust beneath the Proterozoic basins. The high-velocity lower crust in the terrane margin is spatially coincident with crustal wedges recognized in both the active source reflection and receiver function images, which may be typical in convergent continental regions. Along with the isotope evidence that suggests a magmatic arc origin of the deep crust source, the seismic observations favor the operation of a possible Paleoproterozoic subduction process leading the 2.2-Ga Ophthalmia Orogeny (Johnson et al., 2011, 2017).

References

Abbott, D. H., Mooney, W. D., & VanTongeren, J. A. (2013). The character of the Moho and lower crust within Archean cratons and the tectonic implications. *Tectonophysics, 609*, 690–705. https://doi.org/10.1016/j.tecto.2013.09.014

Aitken, A. R. A., Joly, A., Dentith, M. C., Johnson, S. P., Thorne, A. M., & Tyler, I. M. (2013). 3D architecture, structural evolution and mineral prospectivity of the Gascoyne Province, *Geological Survey of Western Australia, Report 123.*

Akaike, H. (1974). A new look at the statistical model identification. *IEEE Transactions on Automatic Control, 19*(6), 716–723. https://doi.org/10.1109/TAC.1974.1100705

Alghamdi, A., Aitken, A., & Dentith, M. (2017). The composition and structure of the deep crust of the Capricorn Orogen. *Australian Journal of Earth Sciences, 65*(1), 9–24. https://doi.org/10.1080/08120099.2018.1389769

Beck, S. L., & Zandt, G. (2002). The nature of orogenic crust in the central Andes. *Journal of Geophysical Research, 107*(B10), 2230. https://doi.org/10.1029/2000JB000124

Bédard, J. H. (2006). A catalytic delamination-driven model for coupled genesis of Archaean crust and sub-continental lithospheric mantle. *Geochimica et Cosmochimica Acta, 70*(5), 1188–1214. https://doi.org/10.1016/j.gca.2005.11.008

Bensen, G. D., Ritzwoller, M. H., & Shapiro, N. M. (2008). Broadband ambient noise surface wave tomography across the United States. *Journal of Geophysical Research, 113*, B05306. https://doi.org/10.1029/2007JB005248

Bodin, T., Sambridge, M., Rawlinson, N., & Arroucau, P. (2012). Transdimensional tomography with unknown data noise. *Geophysical Journal International, 189*, 1536–1556. https://doi.org/10.1111/j.1365-246X.2012.05414.x

Bodin, T., Sambridge, M., Tkal, H., Arroucau, P., Gallagher, K., & Rawlinson, N. (2012). Transdimensional inversion of receiver functions and surface wave dispersion. *Journal of Geophysical Research, 117*, B02301. https://doi.org/10.1029/2011JB008560

Bodin, T., Yuan, H., & Romanowicz, B. (2014). Inversion of receiver functions without deconvolution—Application to the Indian craton. *Geophysical Journal International, 196*(2), 1025–1033. https://doi.org/10.1093/gji/ggt431

Brown, M. (2008). Characteristic thermal regimes of plate tectonics and their metamorphic imprint throughout Earth history: When did Earth first adopt a plate tectonics mode of behavior. *Geological Society of America Special Papers, 440*, 97–128. https://doi.org/10.1130/2008.2440(05)

Cagnard, F., Barbey, P., & Gapais, D. (2011). Transition between "Archaean-type" and "modern-type" tectonics: Insights from the Finnish Lapland Granulite Belt. *Precambrian Research, 187*(1-2), 127–142. https://doi.org/10.1016/j.precamres.2011.02.007

Cawood, P. A., & Tyler, I. M. (2004). Assembling and reactivating the Proterozoic Capricorn Orogen: Lithotectonic elements, orogenies, and significance. *Precambrian Research, 128*(3–4), 201–218. https://doi.org/10.1016/j.precamres.2003.09.001

Chen, Y., Gu, Y. J., Dokht, R. M. H., & Sacchi, M. D. (2015). Crustal imprints of Precambrian orogenesis in western Laurentia. *Journal of Geophysical Research: Solid Earth, 120*, 6993–7012. https://doi.org/10.1002/2014JB011353

Chowdhury, P., Gerya, T., & Chakraborty, S. (2017). Emergence of silicic continents as the lower crust peels off on a hot plate-tectonic Earth. *Nature Geoscience, 10*(9), 698–703. https://doi.org/10.1038/ngeo3010

Christensen, N. I. (1996). Poisson's ratio and crustal seismology. *Journal of Geophysical Research, 101*, 3139–3156. https://doi.org/10.1029/95JB03446

Christensen, N. I., & Mooney, W. (1995). Seismic velocity structure and composition of the continental crust: A global view. *Journal of Geophysical Research, 100*, 9761–9788. https://doi.org/10.1029/95JB00259

Clowes, R. M., Cook, F. A., & Ludden, J. N. (1998). Lithoprobe leads to new perspectives on continental evolution. *GSA Today, 8*(10), 1–7.

De Wit, M. J. (1998). On Archean granites, greenstones, cratons and tectonics: Does the evidence demand a verdict? *Precambrian Research, 91*(1–2), 181–226. https://doi.org/10.1016/S0301-9268(98)00043-6

Deng, Y., Shen, W., Xu, T., & Ritzwoller, M. H. (2015). Crustal layering in northeastern Tibet: A case study based on joint inversion of receiver functions and surface wave dispersion. *Geophysical Journal International, 203*(1), 692–706. https://doi.org/10.1093/gji/ggv321

Dentith, M., Yuan, H., Johnson, S., Murdie, R., & Piña-Varas, P. (2018). Application of deep–penetrating geophysical methods to mineral exploration: Examples from Western Australia. *Geophysics*, *83*(3), WC29–WC41. https://doi.org/10.1190/geo2017-0482.1

DePaolo, D. J., Cerling, T. E., Hemming, S. R., Knoll, A. H., Richter, F. M., Royden, L. R., et al. (2008). Origin and evolution of Earth: Research questions for a changing planet, edited, Rep., National Academy of Sciences.

Du, Z. J., & Foulger, G. R. (1999). The crustal structure beneath the northwest fjords, Iceland, from receiver functions and surface waves. *Geophysical Journal International*, *139*(2), 419–432. https://doi.org/10.1046/j.1365-246x.1999.00945.x

Efron, B., & Tibshitani, R. (1986). Bootstrap methods for standard errors, confidence intervals, and other measures of statistical accuracy. *Statistical Science*, *1*, 54–77.

Fischer, R., & Gerya, T. (2016). Early Earth plume-lid tectonics: A high-resolution 3D numerical modelling approach. *Journal of Geodynamics*, *100*, 198–214. https://doi.org/10.1016/j.jog.2016.03.004

Gessner, K., Yuan, H., Murdie, R., Dentith, M. C., Johnson, S. P., & Brett, J. (2015). The Capricorn Orogen Passive Source Array (COPA) in Western Australia, AGU 2015 Fall Meeting edited, San Francisco.

Gilligan, A., Roecker, S. W., Priestley, K. F., & Nunn, C. (2014). Shear velocity model for the Kyrgyz Tien Shan from joint inversion of receiver function and surface wave data. *Geophysical Journal International*, *199*(1), 480–498. https://doi.org/10.1093/gji/ggu225

Green, P. J. (1995). Reversible jump Markov chain Monte Carlo computation and Bayesian model determination. *Biometrika*, *82*(4), 711–732. https://doi.org/10.1093/biomet/82.4.711

Gu, Y. J., & Shen, L. (2015). Noise correlation tomography of Southwest Western Canada Sedimentary Basin. *Geophysical Journal International*, *202*(1), 142–162. https://doi.org/10.1093/gji/ggv100

Hamilton, W. B. (2007). Earth's first two billion years—The era of internally mobile crust. *Geological Society of America Memoirs*, *200*, 233–296. https://doi.org/10.1130/2007.1200(13)

Hamilton, W. B. (2011). Plate tectonics began in Neoproterozoic time, and plumes from deep mantle have never operated. *Lithos*, *123*(1-4), 1–20. https://doi.org/10.1016/j.lithos.2010.12.007

Hammond, J. O. S., Kendall, J. M., Stuart, G. W., Keir, D., Ebinger, C., Ayele, A., & Belachew, M. (2011). The nature of the crust beneath the Afar triple junction: Evidence from receiver functions. *Geochemistry, Geophysics, Geosystems*, *12*, Q12004. https://doi.org/10.1029/2011GC003738

Hammond, W. C., & Humphreys, E. D. (2000). Upper mantle seismic wave attenuation: Effects of realistic partial melt distribution. *Journal of Geophysical Research*, *105*, 10,987–10,999. https://doi.org/10.1029/2000JB900042

Heinson, G., Boren, G., Ross, G., Campanya, J., Thiel, S., & Selway, K. (2011). The Capricorn Orogen magnetotelluric (MT) transect. In S. Johnson, A. M. Thorne, & I. M. Tyler (Eds.), *Capricorn Orogen seismic and magnetotelluric (MT) workshop 2011* (pp. 75–100). Perth: Geological Survey of Western Australia.

Hyndman, R. D., & Shearer, P. M. (1989). Water in the lower continental crust: Modelling magnetotelluric and seismic reflection results. *Geophysical Journal International*, *98*(2), 343–365. https://doi.org/10.1111/j.1365-246X.1989.tb03357.x

Johnson, S., Thorne, A. M., Tyle, I. M., Korsch, R. J., Kennett, B. L. N., Cutten, H. N. C., et al. (2013). Crustal architecture of the Capricorn Orogen, Western Australia and associated metallogeny. *Australian Journal of Earth Sciences*, *60*(6–7), 681–705. https://doi.org/10.1080/08120099.2013.826735

Johnson, S. P., Korhonen, F. J., Kirkland, C. L., Cliff, J. B., Belousova, E. A., & Sheppard, S. (2017). An isotopic perspective on growth and differentiation of Proterozoic orogenic crust: From subduction magmatism to cratonization. *Lithos*, *268–271*, 76–86. https://doi.org/10.1016/j.lithos.2016.11.003

Johnson, S. P., Sheppard, S., Rasmussen, B., Wingate, M. T. D., Kirkland, C. L., Muhling, J. R., et al. (2011). Two collisions, two sutures: Punctuated pre-1950 Ma assembly of the West Australian Craton during the Ophthalmian and Glenburgh Orogenies. *Precambrian Research*, *189*(3–4), 239–262. https://doi.org/10.1016/j.precamres.2011.07.011

Johnson, T. E., Brown, M., Kaus, B. J. P., & VanTongeren, J. A. (2014). Delamination and recycling of Archaean crust caused by gravitational instabilities. *Nature Geoscience*, *7*(1), 47–52. https://doi.org/10.1038/ngeo2019

Jones, A. G. (1992). Electrical conductivity of the continental lower crust. In D. M. Fountain, R. Arculus, & R. W. Key (Eds.), *Continental lower crust* (pp. 81–143). Amsterdam: Elsevier.

Jones, A. G. (2013). Imaging and observing the electrical Moho. *Tectonophysics*, *609*(0), 423–436. https://doi.org/10.1016/j.tecto.2013.02.025

Julià, J., Ammon, C. J., & Herrmann, R. B. (2003). Lithospheric structure of the Arabian Shield from the joint inversion of receiver functions and surface-wave group velocities. *Tectonophysics*, *371*(1), 1–21. https://doi.org/10.1016/S0040-1951(03)00196-3

Julia, J., Ammon, C. J., Herrmann, R. B., & Correig, A. M. (2000). Joint inversion of receiver function and surface wave dispersion observations. *Geophysical Journal International*, *143*(1), 99–112. https://doi.org/10.1046/j.1365-246x.2000.00217.x

Kennett, B. L. N., Fichtner, A., Fishwick, S., & Yoshizawa, K. (2013). Australian Seismological Reference Model (AuSREM): Mantle component. *Geophysical Journal International*, *192*(2), 871–887. https://doi.org/10.1093/gji/ggs065

Kennett, B. L. N., & Saygin, E. (2015). The nature of the Moho in Australia from reflection profiling: A review. *GeoResJ*, *5*, 74–91. https://doi.org/10.1016/j.grj.2015.02.001

Korhonen, F. J., & Johnson, S. P. (2015). The role of radiogenic heat in prolonged intraplate reworking: The Capricorn Orogen explained? *Earth and Planetary Science Letters*, *428*, 22–32. https://doi.org/10.1016/j.epsl.2015.06.039

Levshin, A. L., Pisarenko, V. F., & Pogrebinsky, G. G. (1972). On a frequency-time analysis of oscillations. *Annales Geophysicae*, *28*, 211–218.

Meissner, R. (1989). Rupture, creep, lamellae and crocodiles: Happenings in the continental crust. *Terra Nova*, *1*(1), 17–28. https://doi.org/10.1111/j.1365-3121.1989.tb00321.x

Menke, W. (1989). *Geophysical data analysis: Discrete inverse theory (revised edition)*. San Diego: Academic.

Moyen, J.-F., & van Hunen, J. (2012). Short-term episodicity of Archaean plate tectonics. *Geology*, *40*(5), 451–454. https://doi.org/10.1130/g322894.1

Murdie, R. E., Yuan, H., Dentith, M. C., Johnson, S. P., & Gessner, K. (2016). Passive seismic studies show configuration of Paleoproterozoic subduction zones and their role in craton assembly in Western Australia. ASEG Extended Abstracts, 1, 1–5.

National Research Council (2012). New Research Opportunities in the Earth Sciences (132 pp.). Washington, DC: The National Academies Press. https://doi.org/10.17226/13236

Nutman, A. P., Friend, C. R. L., & Paxton, S. (2009). Detrital zircon sedimentary provenance ages for the Eoarchaean Isua supracrustal belt southern West Greenland: Juxtaposition of an imbricated ca. 3700Ma juvenile arc against an older complex with 3920–3760Ma components. *Precambrian Research*, *172*(3–4), 212–233. https://doi.org/10.1016/j.precamres.2009.03.019

Occhipinti, S. A., Sheppard, S., Passchier, C., Tyler, I. M., & Nelson, D. R. (2004). Palaeoproterozoic crustal accretion and collision in the southern Capricorn Orogen: The Glenburgh Orogeny. *Precambrian Research*, *128*(3–4), 237–255. https://doi.org/10.1016/j.precamres.2003.09.002

Pilia, S., Rawlinson, N., Cayley, R. A., Bodin, T., Musgrave, R., Reading, A. M., et al. (2015). Evidence of micro-continent entrainment during crustal accretion. *Scientific Reports*, *5*(1), 8218. https://doi.org/10.1038/srep08218

Piña-Varas, P., & Dentith, M. (2017). Magnetotelluric data from the southeastern Capricorn Orogen, Western Australia: An example of widespread out-of-quadrant phase responses associated with strong 3-D resistivity contrasts. *Geophysical Journal International*, *122*, 1022–1032. https://doi.org/10.1093/gji/ggx459

Rawlinson, N., & Sambridge, M. (2005). The fast marching method: An effective tool for tomographic imaging and tracking multiple phases in complex layered media. *Exploration Geophysics*, *36*(4), 341–350. https://doi.org/10.1071/EG05341

Reading, A. M., Tkalčić, H., Kennett, B. L. N., Johnson, S. P., & Sheppard, S. (2012). Seismic structure of the crust and uppermost mantle of the Capricorn and Paterson Orogens and adjacent cratons, Western Australia, from passive seismic transects. *Precambrian Research*, *196–197*, 295–308. https://doi.org/10.1016/j.precamres.2011.07.001

Rudnick, R. L. (1995). Making continental crust. *Nature*, *378*(6557), 571–578. https://doi.org/10.1038/378571a0

Rudnick, R. L., & Fountain, D. M. (1995). Nature and composition of the continental crust: A lower crustal perspective. *Reviews of Geophysics*, *33*, 267–309. https://doi.org/10.1029/95RG01302

Rudnick, R. L., & Gao, S. (2003). 3.01 - composition of the continental crust. In H. D. H. K. Turekian (Ed.), *Treatise on Geochemistry* (pp. 1–64). Oxford: Pergamon. https://doi.org/10.1016/B0-08-043751-6/03016-4

Saito, M. (1988). DISPER80: A subroutine package for the calculation of seismic normal mode solutions. In D. J. Doornbos (Ed.), *Seismological Algorithms: Computational Methods and Computer Programs* (pp. 293–319). New York: Academic Press.

Salmon, M., Kennett, B. L. N., & Saygin, E. (2013). Australian Seismological Reference Model (AuSREM): crustal component. *Geophysical Journal International*, *192*(1), 190–206. https://doi.org/10.1093/gji/ggs004

Sambridge, M., Gallagher, K., Jackson, A., & Rickwood, P. (2006). Trans-dimensional inverse problems, model comparison and the evidence. *Geophysical Journal International*, *167*(2), 528–542. https://doi.org/10.1111/j.1365-246X.2006.03155.x

Saygin, E., & Kennett, B. L. N. (2010). Ambient seismic noise tomography of Australian continent. *Tectonophysics*, *481*(1–4), 116–125. https://doi.org/10.1016/j.tecto.2008.11.013

Saygin, E., & Kennett, B. L. N. (2012). Crustal structure of Australia from ambient seismic noise tomography. *Journal of Geophysical Research*, *117*, B01304. https://doi.org/10.1029/2011JB008403

Selway, K., Sheppard, S., Thorne, A. M., Johnson, S. P., & Groenewald, P. B. (2009). Identifying the lithospheric structure of a Precambrian orogen using magnetotellurics: The Capricorn Orogen, Western Australia. *Precambrian Research*, *168*(3–4), 185–196. https://doi.org/10.1016/j.precamres.2008.09.010

Sheppard, S., Bodorkos, S., Johnson, S. P., Wingate, M. T. D., & Kirkland, C. L. (2010). The Paleoproterozoic Capricorn orogeny: Intracontinental reworking not continent–continent collision, Geological Survey of Western Australia, Report, 108, 33.

Sheppard, S., Occhipinti, S. A., & Tyler, I. M. (2004). A 2005–1970 ma Andean-type batholith in the southern Gascoyne complex, Western Australia. *Precambrian Research*, *128*(3–4), 257–277. https://doi.org/10.1016/j.precamres.2003.09.003

Sizova, E., Gerya, T., & Brown, M. (2014). Contrasting styles of Phanerozoic and Precambrian continental collision. *Gondwana Research*, *25*(2), 522–545. https://doi.org/10.1016/j.gr.2012.12.011

Sizova, E., Gerya, T., Stüwe, K., & Brown, M. (2015). Generation of felsic crust in the Archean: A geodynamic modeling perspective. *Precambrian Research*, *271*, 198–224. https://doi.org/10.1016/j.precamres.2015.10.005

Snelson, C. M., Henstock, T. J., Keller, G. R., Miller Kate, C., & Levander, A. (1998). Crustal and uppermost mantle structure along the deep probe seismic profile. *Rocky Mountain Geology*, *33*(2), 181–198. https://doi.org/10.2113/33.2.181

Snyder, D. B., & Goleby, B. R. (2016). Seismic reflection patterns associated with continental convergent margins through time. *Tectonophysics*, *692*, 3–13. https://doi.org/10.1016/j.tecto.2016.04.027

Stachnik, J. C., Dueker, K., Schutt, D. L., & Yuan, H. (2008). Imaging Yellowstone plume-lithosphere interactions from inversion of ballistic and diffusive Rayleigh wave dispersion and crustal thickness data. *Geochemistry, Geophysics, Geosystems*, *9*, Q06004. https://doi.org/10.1029/2008GC001992

Takeuchi, H., & Saito, M. (1972). Seismic surface waves. In B. A. Bolt (Ed.), *Computational Physics* (pp. 217–295). New York: Academic Press.

Tang, M., Chen, K., & Rudnick, R. L. (2016). Archean upper crust transition from mafic to felsic marks the onset of plate tectonics. *Science*, *351*(6271), 372–375. https://doi.org/10.1126/science.aad5513

Thompson, D. A., Bastow, I. D., Helffrich, G., Kendall, J. M., Wookey, J., Snyder, D. B., & Eaton, D. W. (2010). Precambrian crustal evolution: Seismic constraints from the Canadian shield. *Earth and Planetary Science Letters*, *297*(3–4), 655–666. https://doi.org/10.1016/j.epsl.2010.07.021

Thybo, H., & Artemieva, I. M. (2013). Moho and magmatic underplating in continental lithosphere. *Tectonophysics*, *609*, 605–619. https://doi.org/10.1016/j.tecto.2013.05.032

Van Kranendonk, M. J., Collins, W. J., Hickman, A., & Pawley, M. J. (2004). Critical tests of vertical vs. horizontal tectonic models for the Archaean east Pilbara granite–greenstone terrane, Pilbara craton, Western Australia. *Precambrian Research*, *131*(3–4), 173–211. https://doi.org/10.1016/j.precamres.2003.12.015

VanDecar, J. C., & Crosson, R. S. (1990). Determination of teleseismic relative phase arrival times using multi-channel cross-correlation and least squares. *Bulletin of the Seismological Society of America*, *80*(1), 150–169.

Vanderhaeghe, O. (2009). Migmatites, granites and orogeny: Flow modes of partially-molten rocks and magmas associated with melt/solid segregation in orogenic belts. *Tectonophysics*, *477*(3–4), 119–134. https://doi.org/10.1016/j.tecto.2009.06.021

Wilde, S. A., Valley, J. W., Peck, W. H., & Graham, C. M. (2001). Evidence from detrital zircons for the existence of continental crust and oceans on the Earth 4.4Gyr ago. *Nature*, *409*(6817), 175–178.

Young, M. K., Rawlinson, N., & Bodin, T. (2013). Transdimensional inversion of ambient seismic noise for 3D shear velocity structure of the Tasmanian crust. *Geophysics*, *78*(3), WB49–WB62. https://doi.org/10.1190/geo2012-0356.1

Yuan, H. (2015). Secular change in Archaean crust formation recorded in Western Australia. *Nature Geoscience*, *8*(10), 808–813. https://doi.org/10.1038/ngeo2521

Yuan, H. (2018). High-density Passive-source Seismic (HPS) array in Western Australia. https://doi.org/10.17605/OSF.IO/D82QW

Yuan, H., Johnson, S., Dentith, M., Murdie, R., Gessner, K., Korhonen, F., & Bodin, T. (2017). Seismic structure of a late-Archean microcontinent in the middle of the Western Australian Craton. EGU General Assembly Conference Abstracts, 19, 6126.